A98-31521

ICAS-98-2,8,3

AXISYMMETRIC SIMULATIONS OF TURBULENT COMPRESSIBLE FLOWS OVER AEROSPACE VEHICLES

Cesar A. Buonomo*, Daniel Strauss†
Instituto Tecnológico de Aeronáutica
CTA/ITA/IEAA
12228-900 – São José dos Campos – SP – BRAZIL

João Luiz F. Azevedo‡
Instituto de Aeronáutica e Espaço
CTA/IAE/ASE-N
12228-904 – São José dos Campos – SP – BRAZIL

Abstract

A detailed study of various turbulent flow conditions over the first Brazilian satellite launcher, the VLS, is described. The emphasis of the work is in developing the capability of accurately simulating realistic rocket flowfields, including the effects of the body base and of a propulsive jet, and in understanding the behavior of three turbulence models in such conditions. The flowfields over the VLS at zero angle of attack are modeled by the axisymmetric, thin layer Navier-Stokes equations, and turbulence closure is obtained with the implementation of three different eddy viscosity models. A comparison of the characteristics of these models is performed. Accurate solutions for the transonic and supersonic flight regimes are obtained with emphasis on the vehicle's boundary layer behavior. A study of afterbody flowfields is also included with results for cases with and without propulsive jets.

Introduction

A substantial amount of work has been devoted to the development of reliable computational tools for flow simulation in the context of the aerodynamic and aerothermodynamic design of the VLS system, the first Brazilian satellite launcher. The VLS is a four-stage vehicle in which the first stage is composed of four strap-on boosters around a central core. The vehicle has a hammerhead-type payload shroud which is a configuration known to be prone to flow separation during the transonic flight regime. The experience with similar launchers has shown that the payload acoustic excitation loads due to the separated flow condition in the transonic regime can be as large as those experienced by the payload at take-off. Therefore, there is particular importance in having a thorough understanding of the vehicle's forebody flow condition in this regime. A schematic representation of the VLS system is presented in Fig. 1.

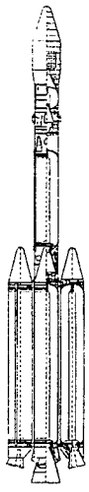

Figure 1: Sketch of the VLS system.

Moreover, the complex plume configuration, which appears for vehicles with such large strap-on boosters, can have an important effect both in terms of the aerodynamics of the vehicle's afterbody as well as in terms of base heating. Hence, the study of the interaction between the external flow and the plumes from the rocket motor nozzles is fundamental for a correct characterization of the flow in the afterbody region. In the context of the present work, a fair amount of effort was also dedicated to standard base flows, i.e., afterbody flows without a propulsive jet. As a consequence, the issues discussed in the paper can also be relevant to afterbody flows likely to be encountered in standard aeronautical system as well as to projectile flows, which are also important to the industry.

Although, clearly, there is interest in studying the flow over the VLS at angle of attack, the present investigation concentrated on axisymmetric calculations. These allow for a far more extensive testing in terms of mesh refine-

*Graduate Student.
†Undergraduate Student.
‡Head, Aeroelasticity & CFD Sections, Space Systems Division.

21st ICAS Congress
13-18 September 1998
Melbourne, Australia

ment and number of different test cases than full 3-D simulations would with the computational resources available at this time. Therefore, the flowfields of interested were modeled by the axisymmetric thin-layer Navier-Stokes equations[1, 2, 3]. The calculations were treated as turbulent in the context of an eddy viscosity turbulence closure model. The Baldwin and Lomax algebraic model[4], the Johnson and King half-equation model[5] and the Baldwin and Barth one-equation model[6] have been used, and their results compared. The governing equations were discretized using the standard Beam and Warming implicit approximate factorization algorithm[7, 8], with the implicit Euler method adopted for the time march and three-point, second-order central difference approximations used for the spatial derivatives.

A multiblock capability was implemented into an existing axisymmetric code[9, 10] with the objective of increasing the code's flexibility in terms of handling more complex configurations or of obtaining a better distribution of grid points. It must be emphasized that, for the present axisymmetric case, the complexity of the geometry is not an overwhelming issue as it could be for realistic 3-D cases. Therefore, one could probably deal with the present problems using a single block grid. However, in the present context, there was interest in developing tools that could be used as building blocks to handle even more complicated configurations in the future. Based on the previous experience of the group, it seemed that the best approach would be to use block structured grids. For easiness of implementation, patched multiblock grids have been preferred at the present stage in this development.

The forthcoming sections will briefly describe the theoretical formulation and numerical implementation details. Several case studies are discussed with emphasis in the forebody flows and, in this context, computational results which are representative of transonic flight conditions are presented and discussed in detail. The most relevant issues investigated in this case were associated with a detailed boundary layer behavior description with emphasis on the separation caused by shock-boundary layer interaction. An assessment of the behavior of the three turbulence models previously mentioned was performed. Mesh refinement studies were also included in the present investigation in an attempt to fully validate the computational capability implemented. Moreover, studies which assessed the effects of the far field boundary position were also performed and are described here. The multiblock extension was initially tested on forebody flow cases for which results were previously available with a single block formulation. After this initial validation, the code was applied to afterbody flow simulation cases, both with and without the presence of nozzle jets.

Theoretical Formulation

The flowfield over the complete VLS vehicle, even at zero angle of attack, is certainly three dimensional. However, the effect of the four strap-on boosters is not considered in the present work. Thus, the azimuthal-invariant, Reynolds-averaged, thin-layer Navier-Stokes equations[1, 2] are employed and, for the case of no body rotation, they can be written in general curvilinear coordinates as

$$\frac{\partial \overline{Q}}{\partial \tau} + \frac{\partial \overline{E}}{\partial \xi} + \frac{\partial \overline{F}}{\partial \eta} + \overline{H} = \frac{M_\infty}{\mathrm{Re}} \frac{\partial \overline{S}}{\partial \eta} \ , \qquad (1)$$

where $\overline{Q}$ is the vector of conserved variables, $\overline{E}$ and $\overline{F}$ are the inviscid flux vectors, $\overline{S}$ is the thin-layer viscous flux vector, and $\overline{H}$ is the axisymmetric source term. A suitable nondimensionalization[8] of the governing equations has been assumed in order to write Eq. (1). The form of the previously defined algebraic vectors can be found, for instance, in Refs. [3] and [11]. In the previous expression, M_∞ is the freestream Mach number and Re is the Reynolds number, which is defined in its usual form as

$$\mathrm{Re} = \frac{\ell \rho_\infty q_\infty}{\mu_\infty} \ , \qquad (2)$$

where ℓ is the reference length, ρ_∞ is the freestream density, q_∞ is the magnitude of the freestream velocity vector, and μ_∞ is the molecular viscosity coefficient at the freestream temperature. Expressions for the required metric terms and for the Jacobian of the coordinate transformation can be found in Refs. [2] and [11], among other references.

The correct account for the viscous effects in the present case involves the implementation of an appropriate turbulence closure model. Three models have been implemented and were tested in this study, the Baldwin and Lomax algebraic model[4], the Johnson and King half-equation model[5] and the Baldwin and Barth one-equation model[6]. For a complete description of these models, the interested reader is referred to the original references previously cited. It is important to emphasize, however, that the specific implementation of the Baldwin and Lomax and the Johnson and King models adopted here is a straightforward extension to the axisymmetric case of the work described in Ref. [12]. Hence, the equations for the Baldwin and Lomax model are the ones widely available in the literature except that, to be consistent with the present nondimensionalization, the expressions for the dimensionless eddy viscosity in the inner and outer regions, respectively, are written as

$$\mu_{t_{\mathrm{inner}}} = \frac{Re}{M_\infty} \rho \ell^2 |\omega| \ , \qquad (3)$$

and

$$\mu_{t_{\mathrm{outer}}} = \frac{Re}{M_\infty} K C_{cp} \rho F_{wake} F_{Kleb} \ . \qquad (4)$$

The definition of the various terms is the standard one for the Baldwin and Lomax model[4]. Moreover, the expressions for the model are implemented in terms of the dimensionless variables and in general curvilinear coordinates, following the work presented in Ref. [13].

The Baldwin and Barth model[6] is a one-equation model which attempts to avoid the need to compute algebraic length scales, without having to resort to more complex two-equation, or k–ϵ type models. The model was

implemented in the present code precisely as described in Baldwin and Barth's original work[6]. The extension of the model for compressible flows was obtained simply by multiplying the kinematic turbulent viscosity coefficient by the local density, as also described in the original reference. Moreover, the turbulence model equation is solved separately from the other governing equations in a loosely coupled fashion. This procedure was adopted in order to avoid having to modify the flux Jacobian matrices and the overall structure of the flow solution algorithm which had been previously implemented[9].

Furthermore, the implementation of both the Baldwin and Lomax and the Baldwin and Barth models has been extended for the multiblock case. This extension has not caused any significant added complexity to the form of implementing these turbulence models, except that some additional care should be exercised when computing distances from a wall in the Baldwin and Lomax case. There was no attempt to extend the implementation of the Johnson and King model to the multiblock case because the present implementation of this model is based upon the Baldwin and Lomax model and the results obtained with the latter for the afterbody test cases were not encouraging, as the paper will show. Moreover, the major interest in using the multiblock capability in the present case was exactly for the simulation of afterbody flows.

Numerical Implementation

The governing equations were discretized in a finite difference context on a structured quadrilateral mesh which would conform to the body. The Beam and Warming implicit approximate factorization scheme[7, 8] was used, with the implicit Euler method selected for the time march. As usual with the Beam and Warming algorithm, the spatial derivatives were centrally differenced using three-point, second-order, finite difference operators. Artificial dissipation terms were added to the formulation in order to control nonlinear instabilities.

Spatial and Temporal Discretization

The finite difference equations resulting from the previously described discretization process can be written as

$$L_\xi L_\eta \Delta_t \overline{Q}^n = R_\xi + R_\eta - \Delta t \overline{H}^n \ . \tag{5}$$

The various operators are defined as

$$\begin{aligned} L_\xi &= I + \Delta t\, \delta_\xi \hat{A}^n - \Delta t\, \varepsilon_I J^{-1} \nabla_\xi \Delta_\xi J \ , \\ L_\eta &= I + \Delta t\, \delta_\eta \hat{B}^n - \Delta t\, \frac{M_\infty}{\mathrm{Re}}\, \overline{\delta}_\eta J^{-1} \hat{M}^n J \\ &\quad -\Delta t\, \varepsilon_I J^{-1} \nabla_\eta \Delta_\eta J \ , \\ R_\xi &= -\Delta t\, \delta_\xi \overline{E}^n + D_\xi \ , \\ R_\eta &= -\Delta t\, \delta_\eta \overline{F}^n + \Delta t\, \frac{M_\infty}{\mathrm{Re}}\, \overline{\delta}_\eta \overline{S}^n + D_\eta \ . \end{aligned} \tag{6}$$

In the above, δ_ξ and δ_η are central difference operators; ∇_ξ and ∇_η are backward difference operators; and Δ_ξ and Δ_η are forward difference operators in the ξ- and η-directions, respectively. The Δ_t is a forward difference operator in time given by

$$\Delta_t \overline{Q}^n = \overline{Q}^{n+1} - \overline{Q}^n \ . \tag{7}$$

The inviscid and viscous flux Jacobian matrices $\hat{A}^n$, $\hat{B}^n$ and $\hat{M}^n$, which appear in the local linearization process, are described in detail in Refs. [11] and [14], and their expressions are not repeated here. The interested reader is referred to these references for the form of these matrices.

The expressions in Eqs. (5) and (6) are indicating that the source term was explicitly implemented, i.e., there is no Jacobian matrix associated with the $\overline{H}$ vector included in the left-hand side operators. Actually, this term was treated both explicitly and implicitly in the present work. There were no apparent differences in the stability characteristics or the convergence rate of the scheme which could be attributed to the different treatment of the source term. Moreover, one should observe that the discretization of the viscous terms uses the so-called midpoint operators, indicated by the $\overline{\delta}_\eta$ operator in Eq. (6). The midpoint operators are used in order to obtain a compact finite difference stencil at each point and to avoid the need for a different discretization of these terms close to computational boundaries. For the left-hand side terms, the use of midpoint operators in the viscous contributions is a necessary condition in order to obtain a tridiagonal linear system and, hence, to obtain a computationally efficient algorithm.

Artificial Dissipation

A central difference approximation is being used in all spatial discretization operators. Hence, artificial dissipation terms must be added to the formulation in order to maintain nonlinear stability. All results reported in the present work have used Pulliam's nonlinear artificial dissipation model[15] for the explicit operators. Therefore, the right-hand side artificial dissipation operators are given by

$$\begin{aligned} D_{\xi_{i,j}} &= \nabla_\xi \left[\left(\sigma_{i+1,j} J^{-1}_{i+1,j} + \sigma_{i,j} J^{-1}_{i,j} \right) \right. \\ &\quad \left. \left(\varepsilon^{(2)}_{\xi_{i,j}} \Delta_\xi J_{i,j} \overline{Q}^n_{i,j} - \varepsilon^{(4)}_{\xi_{i,j}} \Delta_\xi \nabla_\xi \Delta_\xi J_{i,j} \overline{Q}^n_{i,j} \right) \right] \\ D_{\eta_{i,j}} &= \nabla_\eta \left[\left(\sigma_{i,j+1} J^{-1}_{i,j+1} + \sigma_{i,j} J^{-1}_{i,j} \right) \right. \\ &\quad \left. \left(\varepsilon^{(2)}_{\eta_{i,j}} \Delta_\eta J_{i,j} \overline{Q}^n_{i,j} - \varepsilon^{(4)}_{\eta_{i,j}} \Delta_\eta \nabla_\eta \Delta_\eta J_{i,j} \overline{Q}^n_{i,j} \right) \right] \end{aligned} \tag{8}$$

The definition of the various terms which appear in the above equations is discussed in detail in Refs. [15]–[17]. At points adjacent to the computational boundaries, the fourth-difference terms cannot be evaluated. Hence, the operator used at those points is obtained simply by setting $\varepsilon^{(4)}_{i,j}$ to zero.

Implicit artificial dissipation terms were implemented as described in Refs. [16] and [17]. The actual form of the implicit artificial dissipation terms is already shown in Eq. (6). Since the full-block Beam and Warming algorithm is being used in the present case, the computational cost

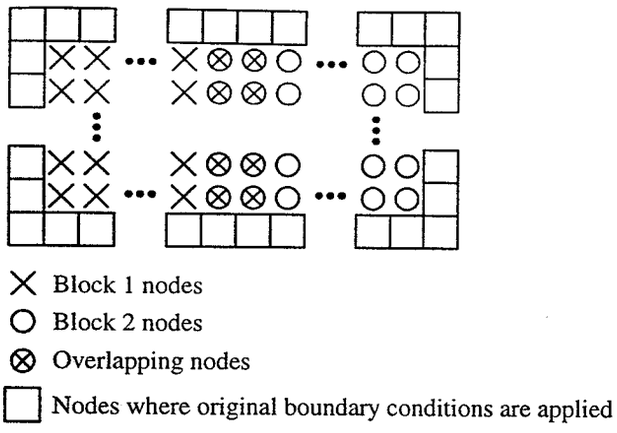

Figure 2: Sketch indicating the communication of information between grid blocks.

of using left-hand side implicit operators equal to those used in the explicit side would be prohibitive. In an attempt to maintain some balance between the amount of implicit and explicit added artificial dissipation, the implicit operator artificial dissipation coefficient is defined as $\varepsilon_I = 3\left(\varepsilon_{i,j}^{(2)} + \varepsilon_{i,j}^{(4)}\right)$. Moreover, observe that this definition guarantees that the amount of added implicit artificial dissipation is never zero.

Multiblock Implementation

As previously discussed, a patched multiblock approach was adopted in this work. The basic ideas underlying the present development were that each block should be able to internally identify the types of boundaries on its four sides and that each side should consist of one single type of boundary. Another basic assumption in the development was that the solution procedure within each block should be implemented in a completely independent fashion. Therefore, additional details of a given configuration could be added on to the simulation simply by creating new grid blocks that would describe such features.

Each computational block has information of the types of boundaries in its four sides, and each side of the block has one single boundary type for all the points along that side. Therefore, the block is operated on using the algorithm previously described and the boundary conditions indicated for its sides. These block boundary conditions are specified through the input file using flags which identify the boundary condition type for each block side. Moreover, the computational meshes are generated such that there is an overlap of two grid points between adjacent grid blocks, as indicated in Fig. 2. This has the objective of facilitating the implementation of internal boundary conditions between blocks at the same time that it allows the solution of the governing equations at every internal grid point.

The important aspect is that the present code only applies the algorithm previously described for interior grid points. Boundary points are always updated through boundary conditions. Hence, with the grid overlap arrangement shown in Fig. 2, the block interfaces are perceived by the block currently being operated as boundaries with Dirichlet-type boundary conditions. The first overlapped point is an interior point of the block being operated. Therefore, the governing equations are solved at this point. The second overlapped point is the actual boundary point of the current block, and its property values are not changed during the current block solution. It should be noted that this second point is an interior point for the other block. Its properties are, therefore, updated through the actual solution of the governing equations when the other block is operated on. After the solution within the block is completed, the information on the first overlapped point is passed on to the neighboring blocks such that their boundary information is updated.

Boundary Conditions

For the axisymmetric simulations, the types of boundary conditions that should be considered include: solid wall, centerline or symmetry, far field, (downstream) exit plane, jet exit, and block interface boundary conditions. The latter were already discussed in the previous section. Wall boundary conditions are obtained by imposing no slip at the wall, zero normal pressure gradient and by assuming the wall to be adiabatic. The centerline, both upstream and downstream of the body, is a singularity of the coordinate transformation in the axisymmetric case. Hence, the governing equations are never solved at the centerline itself. The present approach considers a line of computational points "on the other side" of the centerline in order to impose symmetry boundary conditions.

Far field conditions are treated in two different forms. The initial approach was to simply assume freestream values specified at this computational boundary. Afterwards, non-reflective boundary conditions[18] based on Riemann invariants were used which improved the code's convergence characteristics. Downstream conditions are based on the concept of one-dimensional characteristic relations[16] in order to determine the number of variables which should be extrapolated at this boundary. For a subsonic downstream boundary, the static pressure is fixed and all other quantities at the boundary are obtained by zero-th order extrapolation of their respective values in the adjacent interior point. All flow variables are extrapolated from the adjacent interior point for a supersonic outflow. The jet boundary conditions follow the same reasoning based on characteristic relations. From the point of view of the present computational domain, the jet is seen as a "supersonic" entrance[17], since only sonic and supersonic jets were considered in this work. Hence, all jet properties are specified at the boundary.

Results and Discussion

This section initially presents results for forebody flows over the VLS. The emphasis in this case is in the study of detailed boundary layer behavior and flow separation caused by shock-boundary layer interaction at transonic

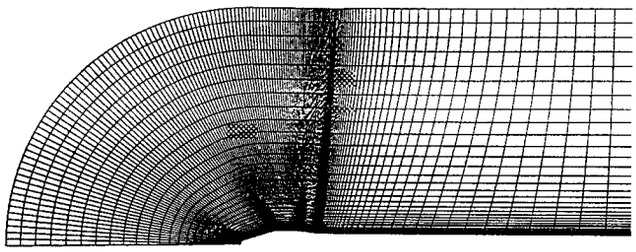

Figure 3: Typical computational mesh (156 × 65 points)

flight conditions. Afterwards, results representative o the multiblock extension are presented for forebody flov cases. The code is finally applied to afterbody flow sim ulation cases.

Analysis of Forebody Flows

Of special interest in the present case, previous work described in Ref. [9] has performed a study of transonic and supersonic flowfields over the VLS at zero angle of attack. In that particular case, the primary concern was the flowfield around the vehicle forebody and the study had been motivated by the need to obtain boundary layer thickness information. The computations performed at that time presented very good agreement with the available experimental data for the majority of the conditions analyzed, except that the transonic case at $M_\infty = 0.90$ seemed to converge to the wrong shock position as the mesh was refined.

The Baldwin and Lomax model[4] was used for the simulations described in Ref. [9] and, therefore, there was a need to explore the same flowfields with more sophisticated turbulence models. Some further work reported in Ref. [10] has concentrated specifically in the transonic regime and analyzed the $M_\infty = 0.90$ case in detail. The study has shown that the results could be significantly improved with more detailed turbulence models and with a closer attention to grid smoothness, particularly in the wall normal direction. In particular, the Johnson and King[5] and the Baldwin and Barth[6] models were implemented and initially tested in the context of the work described in Ref. [10]. The work here described further assessed the behavior of the three turbulence models for such flows.

The computational grids used in the present work were generated algebraically, using the four-surface method as described in Ref. [19]. An example of a typical grid used is shown in Fig. 3. This particular grid has 156 × 65 mesh points. Other meshes were generated, typically increasing the number of grid points in the nominally normal direction, in order to evaluate mesh convergence of the various solutions calculated. Studies which attempted to ascertain the effect of the position of the far field boundary were also performed, and these included computational domain and mesh extensions, together with the appropriate increase in the number of grid points.

The assessment of the predictions of the three turbulence models was performed through comparisons of pressure and eddy viscosity coefficient (μ_t) contours, velocity

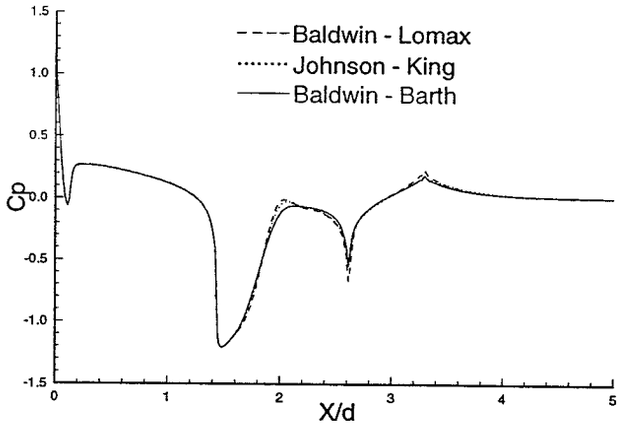

Figure 4: Comparison of pressure coefficient distributions obtained with different turbulence closure models for freestream Mach number $M_\infty = 0.85$ and Re = 20 million.

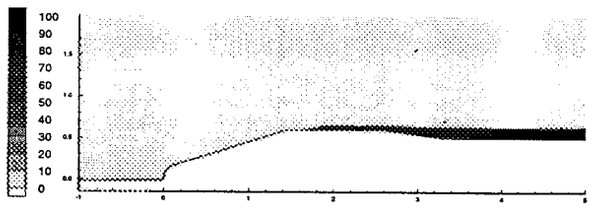

Figure 5: Eddy viscosity coefficient contours for freestream Mach number $M_\infty = 0.85$ obtained with the Baldwin and Barth model (Re = 20 million).

fields and pressure coefficient (Cp) along the body. The simulations considered freestream Mach numbers in the range from $M_\infty = 0.73$ to $M_\infty = 1.05$ for the transonic case. As one can see in Fig. 4, there are no large differences between the pressure coefficient distributions along the body for the solutions with the different turbulence models. This figure shows the results for freestream Mach number $M_\infty = 0.85$ and Reynolds number of 20 million. The same comment would be true if one would look at the pressure contours (not shown) in the field for this case. This trend is observed in the freestream Mach number range of $M_\infty = 0.73$ up to 0.90.

In the same Mach number range, however, it is possible to see large differences in the eddy viscosity coefficient, μ_t, contours computed by the three models. This is evidenced in Figs. 5, 6 and 7. Figure 5 shows the μ_t field obtained in the solution with the Baldwin and Barth model. As one can see, a very smooth and well behaved eddy viscosity coefficient distribution is obtained. It is also possible to observe the thickening of the boundary layer at the shock impingement point along the forebody cylindrical section. Moreover, after the boattail region, the thickness of the region with large values of μ_t remains approximately unchanged.

This is in contrast with the results obtained for this case with the Baldwin and Lomax model, which are shown in Fig. 6. In this latter case, one can also see the boundary layer thickening at the forebody cylindrical section, as expected. However, the eddy viscosity contours

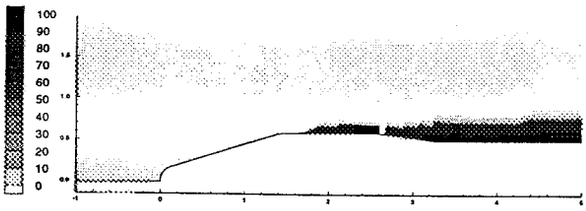

Figure 6: Eddy viscosity coefficient contours for freestream Mach number $M_\infty = 0.85$ obtained with the Baldwin and Lomax model (Re = 20 million).

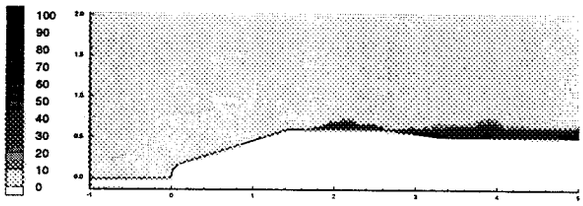

Figure 7: Eddy viscosity coefficient contours for freestream Mach number $M_\infty = 0.85$ obtained with the Johnson and King model (Re = 20 million).

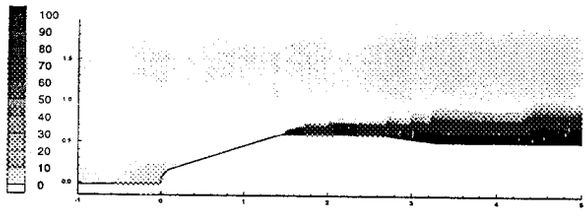

Figure 8: Eddy viscosity coefficient contours for freestream Mach number $M_\infty = 0.73$ obtained with the Baldwin and Lomax model (Re = 20 million).

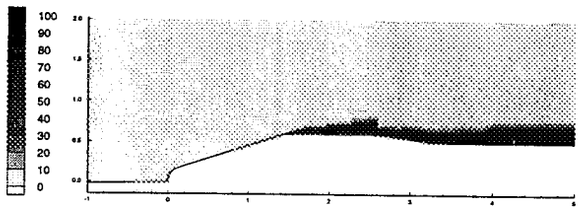

Figure 9: Eddy viscosity coefficient contours for freestream Mach number $M_\infty = 0.73$ obtained with the Johnson and King model (Re = 20 million).

present some discrete jumps in the region downstream of the boattail-afterbody cylinder intersection, which cannot be justified, indicating a fairly erratic behavior of such contours for the solution with the Baldwin and Lomax model. Moreover, the μ_t profile essentially vanishes at the expansion corner of the forebody cylinder-boattail intersection, which is clearly wrong. One should expect some thinning of the boundary layer and, therefore, a reduttion of μ_t levels at such intersection, due to the expansion, but clearly the boundary layer or the turbulent effects cannot completely disappear.

The μ_t distribution obtained with the Johnson and King model can be seen in Fig. 7. As one could expect, the μ_t distribution is smoother than the one obtained with the Baldwin and Lomax model, clearly indicating that the addition of the ODE for the maximum Reynolds stress has incorporated some history effects into the model. The inclusion of the history of the boundary layer development is responsible for the attenuation of the several jumps observed in the Baldwin and Lomax contours downstream of the boattail. However, since the μ_t profile at each longitudinal station is still a Baldwin and Lomax-type profile, modified by a multiplying constant, the problem of vanishing μ_t at expansion corners still exists.

It is important to observe that this anomalous behavior in the eddy viscosity coefficient distribution for the Baldwin and Lomax and the Johnson and King solutions only occurs when the flow is supersonic at the corner. This can be verified by observing the solution for the $M_\infty = 0.73$ case, which is shown in Fig. 8 for the Baldwin and Lomax model and in Fig. 9 for the Johnson and King case. Both figures also show the μ_t contours in the region over the payload fairing. In these cases, the flow is subsonic at the forebody cylinder-boattail intersection and one can see that there is no anomalous behavior of the μ_t distribution at this corner. Moreover, the flow at the forebody cone-cylinder intersection is supersonic in all cases, i.e., Figs. 6–9, and the μ_t distribution vanishes at this supersonic corner for all four solutions. Although this behavior may be difficult to see from Figs. 6–9, because the boundary layer is very thin in the region of interest, an enlarged view (zoom) of the forebody cone-cylinder intersection would clearly show it.

For the case with freestream Mach number $M_\infty = 0.95$ and still considering Re = 20 million, however, significant differences were observed on the wall pressure coefficient distributions calculated with the three turbulence models implemented. These pressure coefficient distributions are shown in Fig. 10. The results with the Baldwin and Barth[6] and the Johnson and King[5] models are indicating a much larger separation region in the boattail than the corresponding results with the Baldwin and Lomax model. The physical explanation for this behavior is quite clear in this case. For the $M_\infty = 0.95$ case, the transonic shock impinges over the body in the boattail region. Therefore, not only this shock is stronger than the one present in the previous cases analyzed, but it also impinges on the body in a region of adverse pressure gradient due to the boattail-afterbody cylinder intersection. Hence, the flow separates at the foot of the shock.

The Baldwin and Lomax model is known to add more μ_t than what would actually be correct. Thus, it tends to numerically prevent the occurence of flow separation or it reduces the extension of the separated region. In this case, the separation is severe enough that even the Baldwin and Lomax model is able to capture it, although its prediction indicates a much smaller separated region. On the other hand, the correction introduced by the Johnson and King model predicts lower levels of μ_t and, therefore, it allows for a more extensive flow separation. The same comment could also be made with regard to the Baldwin and Barth results.

As previously mentioned, typical initial grids used in

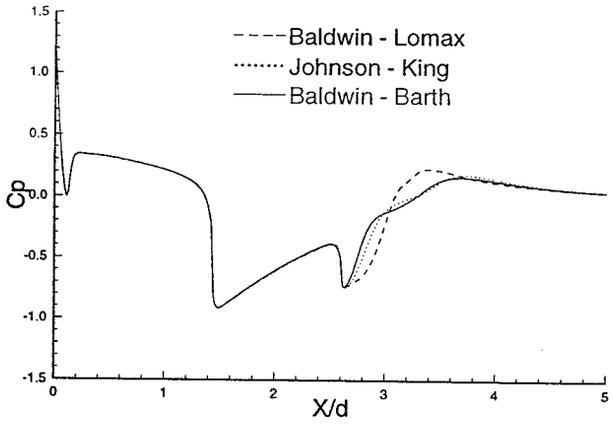

Figure 10: Comparison of pressure coefficient distributions obtained with different turbulence closure models for freestream Mach number $M_\infty = 0.95$ and Re = 20 million.

the present study had 156 × 65 points, and the external boundary was located 10 afterbody diameters away from the body. As the Mach number was increased, the transonic shock on the cylindrical portion of the payload shroud became stronger and it moved downstream. Moreover, a second shock began to form at the wall in the boattail-cylindrical afterbody intersection. These two shocks merge in a λ-type shock, which is stronger and has created the need to extend the position of the far field boundary. Tests were performed with this boundary placed up to 35 afterbody diameters away from the body for these transonic cases. The number of points in the normal direction was increased up to 100 points, in order to maintain the y^+ value of the first point away from the body still small enough while keeping the grid stretching within acceptable levels. An example of the type of problem which can occur if the far field boundary is too close to the body in these cases is shown in Fig. 11. This figure shows results for the $M_\infty = 0.95$ and Re = 20 million case for two different positions of the far field boundary. In the top plot, the far field boundary is located at 10 afterbody diameters from the body whereas, in the bottom plot, it is located at 15 diameters. Clearly, the boundary is causing interference in the pressure contours in the first case. Both calculations shown in Fig. 11 were performed with the Baldwin and Lomax model.

The most critical cases observed considered the freestream Mach numbers $M_\infty = 1.0$ and 1.05, since even solutions with the far field located at 35 body diameters still presented interference in the pressure contours. The obvious solution would be to extend the far field position even further. However, as the far field boundary was placed more than 35 diameters away from the body, the overall point distribution throughout the mesh became too sparse, motivating some modification in the grid topology. This modification consisted in reducing the extension of the computational domain in the upstream direction while extending it in the lateral direction. A typical modified grid used is shown in Fig. 12. Good re-

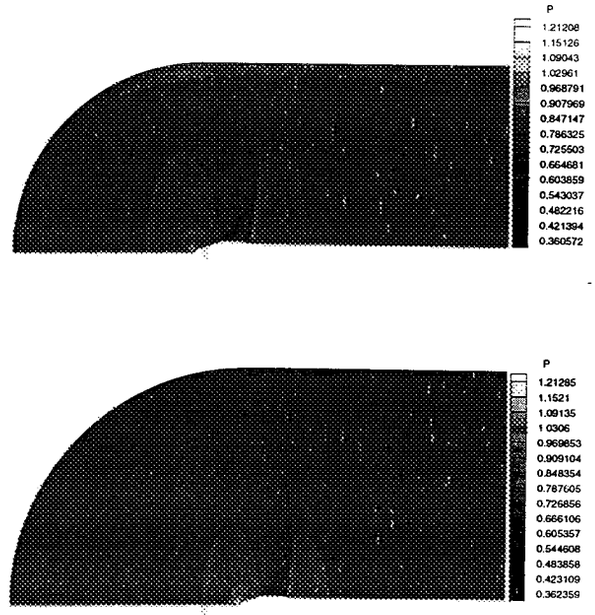

Figure 11: Pressure contours for the $M_\infty = 0.95$ and Re = 20 million case, indicating the effect of the position of the far field boundary. Top plot: far field at 10 diameters; bottom plot: far field at 15 diameters.

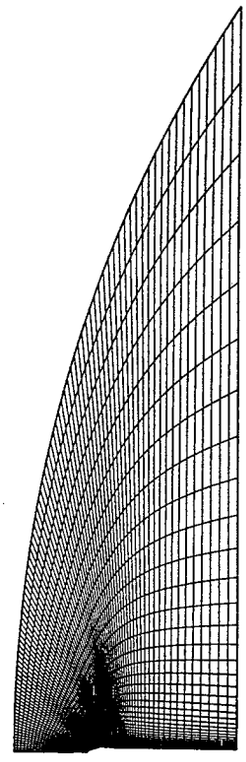

Figure 12: Modified grid topology created to study far field boundary condition interference. Particular grid shown has 93 × 100 points.

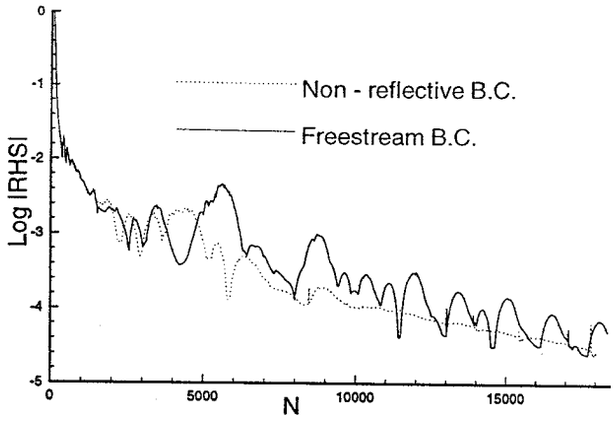

Figure 13: Comparison of maximum residue convergence histories for two different far field boundary condition implementations ($M_\infty = 0.95$ and Re = 20 million).

sults were obtained with the new grid topology for the $M_\infty = 1.05$ case, but the interference was not completely eliminated for the $M_\infty = 1.0$ case.

Another study performed considered the implementation of non-reflective boundary conditions at the far field boundary. These were based on the concept of one-dimensional Riemann invariants and the implementation adopted here closely follows the work reported in Ref. [18]. The basic ideas were to avoid the need of extending the computational boundary further away from the body and to solve the problem at $M_\infty = 1.0$, which could not be solved even with very large meshes, as described. The rationale behind these tests was that the interference problem could be associated with the reflection of outward going waves due to the imposition of fixed (freestream) boundary conditions too close to the body. Therefore, the implementation of non-reflective conditions could help minimize such effects.

Unfortunately, little was accomplished in this sense, because the authors were not able to significantly reduce the computational domain with the adoption of such boundary conditions and there was still a problem with the $M_\infty = 1.0$ case. However, the use of non-reflective boundary conditions has yielded an improvement in the smoothness of the code's convergence history, as one can see in Fig. 13. This seems to be an indication that non-reflective boundary conditions have indeed allowed for a more correct treatment of the outward going waves and, therefore, they have increased the robustness of the code.

On the other hand, this also indicates that the previous anomalies observed in the pressure contours, when the boundary was too close to the body, were the result of the extension of transonic perturbations reflected back into the flowfield. Hence, especially for the most critical cases, there is a need to treat the far field boundary conditions in an optimum way. Boundary conditions were implemented in this work in an explicit fashion. Therefore, there is a time lag between the solution update for the interior points and that for the boundary points, which should be the most relevant aspect causing the reflection.

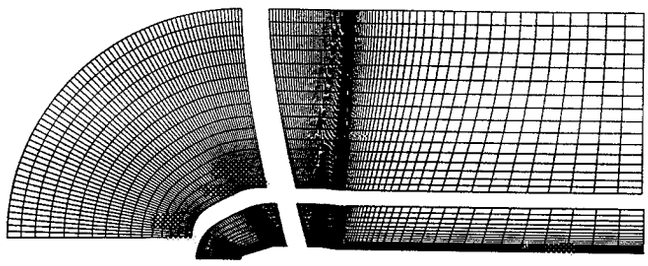

Figure 14: Four-block grid for the VLS forebody.

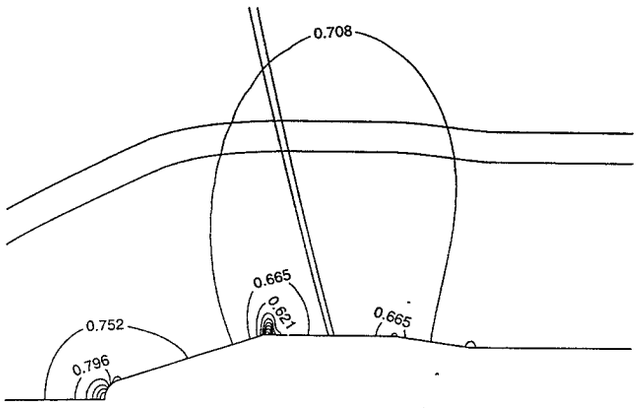

Figure 15: Pressure contours over the VLS forebody for $M_\infty = 0.73$. Simulation uses a four-block grid. Figure also shows block interface lines.

An optimum treatment of the far field boundary conditions should consider an implicit implementation of such conditions for this case.

Multiblock Extension

The first tests performed with the multiblock capability were an attempt to reproduce results which were previously calculated[10] with the single block code, in order to validate the present implementation. These are results for the forebody portion of the vehicle and the single block grid used in these calculations has been already shown in Fig. 3. Multiblock computations have been performed for this configuration using two blocks and using four blocks. The four-block results will be presented here. The computational mesh for this case is shown in Fig. 14. This mesh is essentially equivalent to the one presented in Fig. 3, except that it is topologically divided into four blocks. Fig. 14 shows these blocks separated solely to facilitate the reader's understanding of the block breakup. Simulations for freestream Mach numbers of 0.5 and 0.73 were performed with the four-block grid. All forebody computations used for comparison in the present case were performed with the Baldwin and Lomax[4] algebraic eddy viscosity model.

Results for the $M_\infty = 0.73$ case are shown in Fig. 15 in terms of pressure contours. The Reynolds number for this calculation was 20 million, based on the afterbody diameter. One can observe from Fig. 15 that there is very good continuity of pressure contour lines across block interfaces. Incidentally, the block interfaces with their two

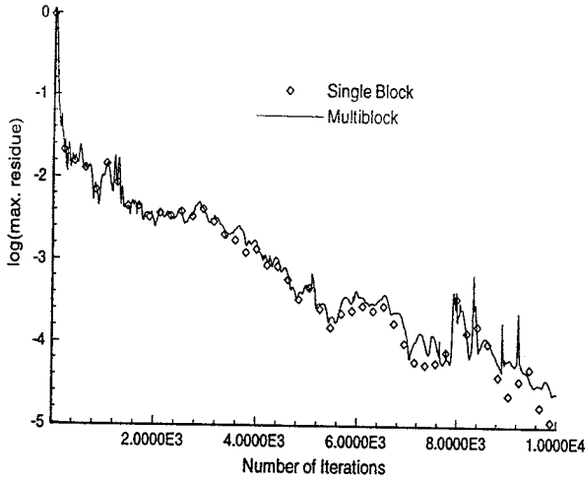

Figure 16: Comparison of single block and multiblock convergence histories ($M_\infty = 0.73$, $Re = 20 \times 10^6$).

overlapped points are also indicated in Fig. 15. The good continuity characteristics of the property contour lines across block interfaces is an indication of the correction and efficiency of the communication between computational blocks.

The pressure coefficient distributions along the body for the respective freestream Mach number cases, either with two or with four blocks, are completely identical to the single block solution. These results indicate that, at least for the forebody flow cases analyzed, the need to pass information across blocks has not caused any deterioration in the numerical solution. Moreover, the convergence rate of the multiblock solution is completely equivalent to that observed with the single block case. This can be clearly seen from Fig. 16, which shows the convergence history for the $M_\infty = 0.73$ case with single and with multiple block grids. Both computations were run with the same CFL number, using a variable time step option available in the code. The results in Fig. 16 are indicating that the explicit treatment of the internal boundary conditions is not reducing the rate of convergence to steady state in this case. Furthermore, this is an indication that the present multiblock implementation does not cause any degradation in the level of solution convergence possible with the algorithm.

A Study of Afterbody Flows

The previous results provided confidence in the correct implementation of the multiblock procedure in the present case. Therefore, the forthcoming tests will consider afterbody flows. A typical multiblock mesh used for the afterbody flow simulations is shown in Fig. 17. This particular grid is composed of four blocks. The first two blocks comprise the complete vehicle up to the base, the third block includes the region from the vehicle base until the downstream boundary, with a "height" equal to the base height, and the fourth block completes the computational domain in this case.

An indication of the solution improvement obtained by the use of multiblock grids, for these afterbody cases, is

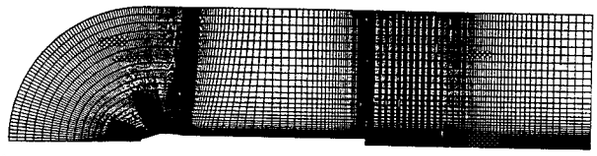

Figure 17: A typical multiblock grid used for the afterbody flow simulations.

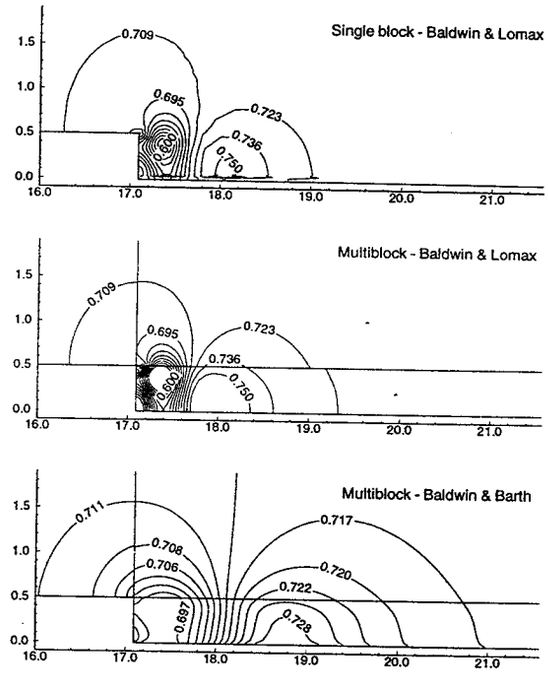

Figure 18: Pressure contours in the base region for $M_\infty = 0.5$ and $Re = 20 \times 10^6$. Results shown: **(a)** single block; **(b)** multiblock with the Baldwin and Lomax model; and **(c)** multiblock with the Baldwin and Barth model.

shown in Fig. 18. This figure compares the solution on a single block grid, following the work described in Ref. [20], with the solution on the four block grid presented in Fig. 17, for the case without a propulsive jet. These figures present pressure contours at the base and near wake regions for a freestream Mach number $M_\infty = 0.5$ and a Reynolds number of 20 million, based on the afterbody diameter. Both results with the Baldwin and Lomax and with the Baldwin and Barth models are presented for the multiblock case.

The multiblock calculations yielded an increased resolution of the flow features in the vicinity of the vehicle base, and the results with the Baldwin and Barth model indicate a more correct position for the rear stagnation point according to available experimental data[21]. It is interesting to observe that the results in the top and middle plots in Fig. 18, although being calculated on very different meshes, have the same overall appearance. Obviously, the middle plot provides a much better resolution of flow features due to the use of the multiblock grid. On the other hand, the middle and bottom plots were calculated on the same mesh, and the results are clearly

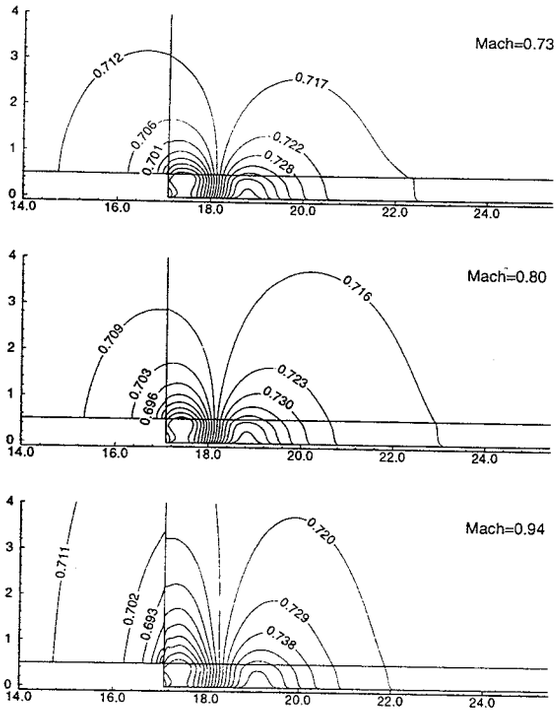

Figure 19: Pressure contours in the base region for different Mach numbers and $Re = 20 \times 10^6$. All computations use the Baldwin and Barth model.

quite different. The conclusion is that, aside from the obvious quality in the definition of the results which is clearly influenced by the mesh, the factor which is really defining the topology of the flow is the turbulence model. As indicated, the Baldwin and Barth results have better agreement with the experimental data, as one could expect considering the results previously shown for forebody flows.

Several other cases were run for this all-base afterbody configuration. The results for some of these cases are shown in Fig. 19, which presents dimensionless pressure contours in the near-wake region. In particular, this figure shows the results for $M_\infty = 0.73$, 0.80 and 0.94. All of these cases used the Baldwin and Barth turbulence closure model and assumed a Reynolds number of 20 million based on the afterbody diameter. The results reproduce the general trend of the expected behavior and provide good agreement, in terms of rear stagnation point position, with data available in the literature[21]. As in previous figures, the block interface lines are shown in Fig. 19 in order to indicate the good contour continuity across such interfaces.

Pressure contours for a supersonic case with freestream Mach number $M_\infty = 2.5$ are shown in Fig. 20. The figure shows most of the complete computational domain, including the vehicle forebody. The more relevant features of this flowfield are evident from Fig. 20. Finally, results with a propulsive jet are shown in Fig. 21 in terms of Mach number contours in the wake/plume region. The freestream conditions in this case are given by $M_\infty = 0.5$ and $Re = 20 \times 10^6$. The jet conditions are $M_{jet} = 1.0$,

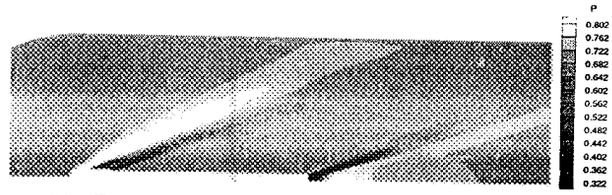

Figure 20: Pressure contours for the $M_\infty = 2.5$ and $Re = 20 \times 10^6$ case for the configuration with a power-off base.

Figure 21: Mach number contours in the wake/plume region for the case with a propulsive jet ($M_\infty = 0.5$, $Re = 20 \times 10^6$, $M_{jet} = 1.0$, $p_{jet} = 3p_\infty$ and $T_{jet} = 2T_\infty$).

$p_{jet} = 3p_\infty$ and $T_{jet} = 2T_\infty$. Although this figure only shows the afterbody portion of the flow, it should be emphasized that the computation considers the complete vehicle as in the previous cases. The structure of the flowfield in the vicinity of the jet exit is well defined and it is in agreement with the expected results for this case.

Concluding Remarks

The paper presented a study of turbulent flowfields over the first Brazilian satellite launcher, the VLS. The work was performed in the context of developing computational tools that could be routinely used for the prediction of aerodynamic characteristics of the VLS and similar vehicles. The flowfields of interest were simulated using the axisymmetric Reynolds-averaged Navier-Stokes equations with the addition of appropriate eddy viscosity-type turbulence closure models. Three different turbulence models were implemented and tested. A patched multiblock version of code was developed and it was shown to exactly reproduce forebody flow results which had been previously calculated with the single block code.

The computational results have indicated that there are no large differences between the pressure coefficient distributions on the body, obtained with the different models, provided that the flow remains attached. However, the results have also shown that, even for these cases in which the pressure distributions are essentially identical, there are large differences in the distribution of the eddy viscosity coefficient, μ_t, in the field. The μ_t behavior for the Baldwin and Barth predictions is smoother and more consistent with the expected results than the ones obtained with the other models. In particular, the μ_t distribution calculated by the Baldwin and Lomax model is fairly erratic, which is a direct consequence of the use of only local information in the construction of the model.

For the cases with flow separation, the predictions obtained with the Baldwin and Barth model are substantially better than those offered by the algebraic model, even in terms of pressure coefficient distributions. For

wall bounded shear layers, this difference seems to be basically associated with the ability of determining the onset of flow separation. Since the Baldwin and Lomax model adds more μ_t to the solution, this has a tendency of delaying, or even eliminating, flow separation. For wake flows, clearly there was not much hope that the algebraic model could adequately handle the situation. The present computational results have confirmed this expectation and, for the afterbody flows, the best comparison with the available data was obtained with the solutions with the Baldwin and Barth model.

Acknowledgments

The present work was partially supported by Conselho Nacional de Desenvolvimento Científico e Tecnológico, CNPq, under the Integrated Project Research Grant No. 522413/96-0.

References

1. Nietubicz, C.J., Pulliam, T.H., and Steger, J.L., "Numerical Solution of the Azimuthal-Invariant Thin-Layer Navier-Stokes Equations," AIAA Paper 79-0010, 17th Aerospace Sciences Meeting, New Orleans, LA, Jan. 1979.
2. Deiwert, G.S., "Supersonic Axisymmetric Flow over Boattails Containig a Centered Propulsive Jet," *AIAA Journal*, Vol. 22, No. 10, Oct. 1984, pp. 1358-1365.
3. Zdravistch, F., and Azevedo, J.L.F., "Numerical Simulation of High Speed Flows Over Complex Satellite Launchers," *Proceedings of the 3rd Brazilian Thermal Sciences Meeting*, Vol. I, Itapema, SC, Brazil, Dec. 1990, pp. 233-238.
4. Baldwin, B.S., and Lomax, H., "Thin Layer Approximation and Algebraic Model For Separated Turbulent Flows," AIAA Paper 78-257, Huntsville, Ala., 1978.
5. Johnson, D.A., and King, L.S., "A Mathematically Simple Turbulence Closure Model for Attached and Separated Turbulent Boundary Layers," *AIAA Journal*, Vol. 23, No. 11, Nov. 1985, pp. 1684-1692.
6. Baldwin, B.S., and Barth, T.L., "A One-Equation Turbulence Transport Model for High Reynolds Number Wall-Bounded Flows," NASA TM-102847, 1990.
7. Beam, R.M., and Warming, R.F., "An Implicit Factored Scheme for the Compressible Navier-Stokes Equations," *AIAA Journal*, Vol. 16, No. 4, April 1978, pp. 393-402.
8. Pulliam, T.H., and Steger, J.L., "Implicit Finite-Difference Simulations of Three-Dimensional Compressible Flow," *AIAA Journal*, Vol. 18, No. 2, Feb. 1980, pp. 159-167.
9. Azevedo, J.L.F., Menezes, J.C.L., and Fico, N.G.C.R., Jr., "An Assessment of Boundary Layer Properties for Transonic and Supersonic Flows Over the VLS," AIAA Paper 95-1769-CP, *Proceedings of the 13th AIAA Applied Aerodynamic Conference*, Part 1, San Diego, CA, 1995, pp. 41-51.
10. Azevedo, J.L.F., Menezes, J.C.L., and Fico, N.G.C.R., Jr., "Accurate Turbulent Calculations of Transonic Launch Vehicle Flows," AIAA Paper No. 96-2484-CP, *Proceedings of the 14th AIAA Applied Aerodynamics Conference*, Part 2, New Orleans, LA, June 1996, pp. 841-851.
11. Fernández, F.Z., "Simulation of Aerodynamic Flows Over Cluster Type Configurations," Master Dissertation, Instituto Tecnológico de Aeronáutica, São José dos Campos, SP, Brazil, Nov. 1990 (in Portuguese).
12. Menezes, J.C.L., "Numerical Analysis of Transonic Turbulent Flows About Airfoils," Master Dissertation, Instituto Tecnológico de Aeronáutica, São José dos Campos, SP, Brazil, July 1994 (in Portuguese).
13. Shirazi, S.A., and Truman, C.R., "A Study of Algebraic and Half-Equation Turbulence Models for Hypersonic PNS Predictions," AIAA Paper 88-0222, AIAA 26th Aerospace Sciences Meeting, Reno, NV, Jan. 1988.
14. Pulliam, T.H., and Steger, J.L., "Recent Improvements in Efficiency, Accuracy and Convergence for Implicit Approximate Factorization Algorithms," AIAA Paper 85-0360, AIAA 23rd Aerospace Sciences Meeting, Reno, Nevada, Jan. 1985.
15. Pulliam, T.H., "Artificial Dissipation Models for the Euler Equations," *AIAA Journal*, Vol. 24, No. 12, Dec. 1986, pp. 1931-1940.
16. Azevedo, J.L.F., Fico, N.G.C.R., Jr., Ortega, M.A., and Luna, G.C., "Nozzle Flow Computations Using the Euler Equations," *Proceedings of the 18th Congress of the International Council of the Aeronautical Sciences*, Vol. 1, Beijing, China, 1992, pp. 97-107.
17. Azevedo, J.L.F., Fico, N.G.C.R., Jr., and Ortega, M.A., "Two-Dimensional and Axisymmetric Nozzle Flow Computations Using the Euler Equations," *Journal of the Brazilian Society of Mechanical Sciences*, Vol. 17, No. 2, Oct. 1995, pp. 147-170.
18. Azevedo, J.L.F., and Oliveira, L.C., "Unsteady Airfoil Flow Simulations Using the Euler Equations," AIAA Paper 94-1892-CP, *Proceedings of the 12th AIAA Applied Aerodynamics Conference*, Part 2, Colorado Springs, CO, June 1994, pp. 650-660.
19. Fletcher, C.A.J., *Computational Techniques for Fluid Dynamics. 2 - Specific Techniques for Different Flow Categories*, Springer-Verlag, New York, 1988.
20. Gregório, E.L., "Numerical Simulation of Flows in the Afterbody Region of Launch Vehicles," Graduation Project, Dept. of Aeronautical Engineering, Instituto Tecnológico de Aeronáutica, São José dos Campos, SP, Brazil, Nov. 1995 (in Portuguese).
21. Merz, R.A., Page, R.H., and Przirembel, C.E.G., "Subsonic Axisymmetric Near-Wake Studies," *AIAA Journal*, Vol. 16, No. 7, July 1978, pp. 656-662.